IUCrJ
ISSN 2052-2525
BIOLOGY | MEDICINE

Room-temperature photo-induced martensitic transformation in a protein crystal. Corrigendum

Steven Dajnowicz,[a,b] Patricia S. Langan,[b]‡ Kevin L. Weiss,[b] Ilia N. Ivanov[c] and Andrey Kovalevsky[b]*

[a]Department of Chemistry and Biochemistry, University of Toledo, Toledo, Ohio 43606, USA, [b]Neutron Scattering Division, Oak Ridge National Laboratory, Oak Ridge, Tennessee 37831, USA, and [c]Center for Nanophase Materials Sciences, Oak Ridge National Laboratory, Oak Ridge, Tennessee 37831, USA. *Correspondence e-mail: kovalevskyay@ornl.gov

‡ Present address: Lentigen Technology, Gaithersburg, Maryland 20878, USA

Keywords: martensitic transformations; reversibly switchable fluorescent proteins; fluorescence; tetramerization; isomerization; chromophore deprotonation; UV–vis absorption spectroscopy; room-temperature X-ray photocrystallography

The article by Dajnowicz *et al.* [*IUCrJ* (2019). **6**, 619–629] is withdrawn.

Since acceptance for publication, the authors of Dajnowicz *et al.* (2019) have become aware that, while the data presented regarding the crystal structures, UV–Vis and fluorescence spectra are correct, the authors cannot conclude with certainty that the photo-induced structural changes can occur *in crystallo*, *i.e.* as a martensitic transformation. The article has therefore been withdrawn.

References

Dajnowicz, S., Langan, P. S., Weiss, K. L., Ivanov, I. N. & Kovalevsky, A. (2019). *IUCrJ* **6**, 619–629.

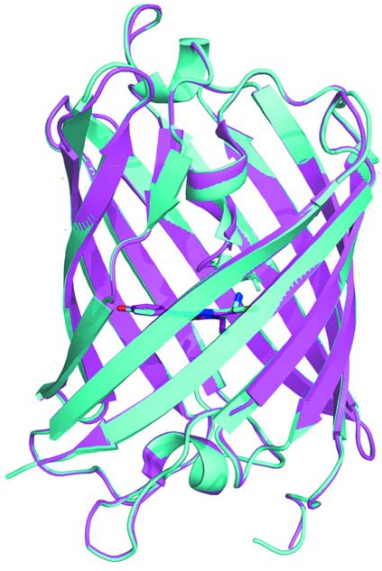

IUCrJ
ISSN 2052-2525
BIOLOGY | MEDICINE

Room-temperature photo-induced martensitic transformation in a protein crystal

Steven Dajnowicz,[a,b] Patricia S. Langan,[b]‡ Kevin L. Weiss,[b] Ilia N. Ivanov[c] and Andrey Kovalevsky[b]*

[a]Department of Chemistry and Biochemistry, University of Toledo, Toledo, Ohio 43606, USA, [b]Neutron Scattering Division, Oak Ridge National Laboratory, Oak Ridge, Tennessee 37831, USA, and [c]Center for Nanophase Materials Sciences, Oak Ridge National Laboratory, Oak Ridge, Tennessee 37831, USA. *Correspondence e-mail: kovalevskyay@ornl.gov

Received 21 January 2019
Accepted 26 April 2019

Edited by J. Trewhella, University of Sydney, Australia

‡ Present address: Lentigen Technology, Gaithersburg, Maryland 20878, USA

Keywords: martensitic transformations; reversibly switchable fluorescent proteins; fluorescence; tetramerization; isomerization; chromophore deprotonation; UV–vis absorption spectroscopy; room-temperature X-ray photocrystallography.

PDB references: dTetdron at equilibrium, 6myb; hTetdron at equilibrium, 6mxw; 400nm irradiated dTetdron, 6myc

Supporting information: this article has supporting information at www.iucrj.org

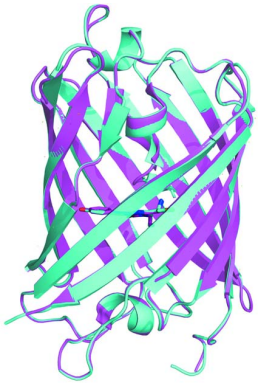

Martensitic transformations are the first-order crystal-to-crystal phase transitions that occur mostly in materials such as steel, alloys and ceramics, thus having many technological applications. These phase transitions are rarely observed in molecular crystals and have not been detected in protein crystals. Reversibly switchable fluorescent proteins are widely used in biotechnology, including super-resolution molecular imaging, and hold promise as candidate biomaterials for future high-tech applications. Here, we report on a reversibly switchable fluorescent protein, Tetdron, whose crystals undergo a photo-induced martensitic transformation at room temperature. Room-temperature X-ray crystallography demonstrates that at equilibrium Tetdron chromophores are all in the *trans* configuration, with an ∼1:1 mixture of their protonated and deprotonated forms. Irradiation of a Tetdron crystal with 400 nm light induces a martensitic transformation, which results in Tetdron tetramerization at room temperature revealed by X-ray photocrystallography. Crystal and solution spectroscopic measurements provide evidence that the photo-induced martensitic phase transition is coupled with the chromophore deprotonation, but no *trans–cis* isomerization is detected in the structure of an irradiated crystal. It is hypothesized that protein dynamics assists in the light-induced proton transfer from the chromophore to the bulk solvent and in the ensuing martensitic phase transition. The unique properties of Tetdron may be useful in developing novel biomaterials for optogenetics, data storage and nanotechnology.

1. Introduction

Martensitic transformations are diffusionless first-order crystal-to-crystal phase transitions in which the original crystal lattice distorts after the application of a stimulus. Martensitic materials include stiff engineering materials such as metals, alloys and ceramics (Christian, 2002), and some molecular crystals (Mnyukh *et al.*, 1975; Anwar *et al.*, 2007). In these materials, such transformations are usually induced (or stimulated) by temperature changes, transforming one crystal form into another, and can be irreversible, as seen in steels, or reversible, as observed in shape-memory alloys and small-molecule crystals (Anwar *et al.*, 2007; Otsuka & Wayman, 1998). Martensitic transformations can also occur in proteins, with the most noteworthy example being the injection mechanism of the T4 bacteriophage. During the virus attack on a bacterium the tail-sheath-protein assembly of the bacteriophage contracts to about a third of its initial length through an irreversible martensitic phase change to puncture the bacterial membrane and subsequently inject its DNA into the bacterial interior (Olson & Hartman, 1982; Falk & James, 2006). Martensitic transformations have numerous techno-

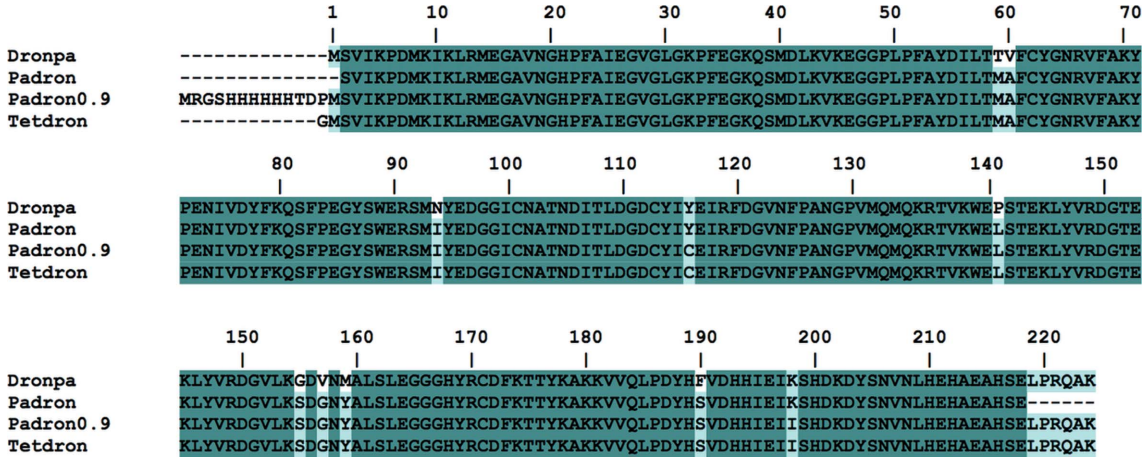

Figure 1
Amino-acid sequence alignment of Dronpa, Padron, Padron0.9 and Tetdron.

logical applications and are of substantial importance in developing new materials possessing shape memory, superelasticity and self-healing properties (Otsuka & Wayman, 1998; Kelley & Rose, 2002). Another interesting application of martensitic materials based on proteins is using them as molecular nanomachines (Bhattacharya & James, 2005). However, to the best of our knowledge, no martensitic transformation has been observed in an actual protein crystal and no crystal structures of the two pertinent phases have been determined so far.

Fluorescent proteins (FPs) have been continuously engineered to possess distinctive photo-physical properties for applications in molecular and cellular biology (Zimmer, 2002) since their discovery in 1962 (Shimomura *et al.*, 1962). The characteristic FP contains a β-barrel fold with short α-helical sections capping each end of the barrel. During the folding process of an FP, a chromophore is formed internally and auto-catalytically through a sequential cyclization–oxidation–dehydration chemical reaction involving a tripeptide within the protein sequence (Zimmer, 2002; Tsien, 1998; Remington, 2006). The formation of the chromophore within the protein matrix enhances the emission of light upon illumination. The ability to genetically encode proteins into cells allows FPs to be used as biomarkers and sensors. For example, the green FP has been manipulated to acquire better pH and redox-sensing properties inside cells (Kneen *et al.*, 1998; Miesenböck *et al.*, 1998; Campbell *et al.*, 2018). Generally, rational protein engineering or directed evolution approaches have been employed to obtain desired or improved functionalities of FPs. To take full advantage of rational protein engineering, a deep understanding of the physico-chemical determinants that influence the photo-physical properties of FPs is needed to develop biomaterials based on these proteins. However, complete understanding of the molecular determinants that govern the photo-physical and photo-chemical properties is challenging because of the intrinsic complexity of the protein matrix. Despite many years of research, the connection between the protein dynamics and proton transfer that contribute to the photo-physical properties of FPs are still not well understood.

Recently, FPs that possess fluorescent properties controllable by irradiation with UV or visible light have been discovered (Ando *et al.*, 2004; Andresen *et al.*, 2008; Adam *et al.*, 2008; Langan *et al.*, 2016). Three classes of such photo-switchable FPs have emerged: (1) photo-activatable FPs, which irreversibly convert to a fluorescent state upon irradiation; (2) photo-convertible FPs, in which the emitting wavelength can be altered upon irradiation; and (3) reversibly switchable FPs (RSFPs), which can be switched repeatedly between a non-fluorescent 'off' state and a fluorescent 'on' state by irradiating the protein with light of two distinctive wavelengths. RSFPs have gained attention from their utilization in nanoscopy, contrast-enhancing imaging applications, and future data-writing and storage devices (Chang *et al.*, 2012; Zhou & Lin, 2013). Consequently, the molecular mechanism that drives the photo-switching process has been of great interest (Duan *et al.*, 2014). RSFPs can be further categorized into two groups – positive and negative RSFPs. Positive RSFPs are characterized by having an equilibrium dark non-fluorescent state that can be switched 'on' to a fluorescent state upon irradiation; whereas negative RSFPs are characterized by having an equilibrium fluorescent state that can be switched 'off' upon irradiation to a dark non-fluorescent state. This photo-switching behaviour is usually caused by a *cis–trans* isomerization of the chromophore accompanied by the excited-state proton transfer (ESPT) that is induced by illumination of the protein. For example, Dronpa – a negative RSFP – exhibits a fluorescent state at equilibrium, in which the chromophore is in the *cis* configuration containing an anionic benzylidene phenolate moiety (Campbell *et al.*, 2018; Habuchi *et al.*, 2005; Andresen *et al.*, 2007). Upon irradiation of Dronpa with 488 nm light, its chromophore is converted to the *trans* configuration and the neutral form of the benzylidene phenol moiety, resulting in a non-fluorescent state. In contrast, Padron and Padron0.9, which contain eight and ten amino-acid substitutions relative to Dronpa (Fig. 1), possess positive photo-switching characteristics (Andresen *et al.*, 2008; Brakemann *et al.*, 2010; Walter *et al.*, 2015). The dark non-fluorescent state with the anionic

chromophore in the *trans* configuration is observed for both Padron and Padron0.9 at equilibrium (Brakemann *et al.*, 2010; Regis Faro *et al.*, 2011). Upon irradiation with 500 nm light, the chromophore is fully converted to the *cis* configuration, with a portion of the chromophores becoming protonated and the remaining anionic chromophore portion emitting ∼525 nm light. Therefore, it appears that the tuning of the *cis*–*trans* equilibria and the proton-transfer dynamics of the chromophore influence photo-switchable and photo-chromic behaviours of these proteins.

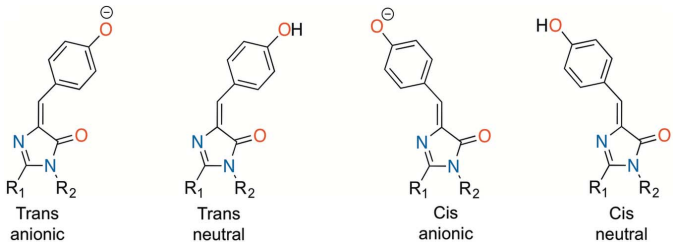

Here, we report on the unique photo-physical properties of an RSFP Tetdron, which is a variant of Padron0.9. We discovered that crystals of Tetdron can undergo a martensitic transformation triggered by illumination with UV light. At equilibrium, UV–vis absorption spectra provided evidence that Tetdron contains a mixture of the anionic and neutral forms of the chromophore both in solution and in the solid state, whereas the room temperature X-ray structure indicated the chromophore adopts only the *trans* configuration. Upon irradiation of a Tetdron crystal with 400 nm light at room temperature into the absorption band of the protonated chromophore, it undergoes a photo-induced martensitic transformation which results in tetramerization of the protein *in crystallo* accompanied only by the chromophore deprotonation demonstrated by the disappearance of the protonated-chromophore absorption band. We observed no changes in the local structure and hydrogen-bonding networks near the chromophore in the X-ray photo-crystallographic structure obtained from the illuminated crystal. Rather, large-scale changes of the unit cell and crystal packing were triggered. To the best of our knowledge, this is the first time such a crystal-to-crystal phase transition induced by light is detected for an RSFP or any other protein crystal. Our results demonstrate that RSFPs can be further explored for applications beyond those currently known and provide an excellent testbed for developing new biomaterials for optogenetics, optical data storage and nanodevices.

2. Results

2.1. Tetdron crystal irradiation with 400 nm light causes a martensitic transformation

Tetdron is a derivative of Padron0.9, having the same two amino acid substitutions Y166C and K198I compared with the parent Padron (Fig. 1). Unlike Padron0.9, Tetdron lacks the His-tag and a linker at its N-terminus, having only an extra Gly residue. Tetdron crystallizes in a monoclinic space group ($P2_1$) with eight independent molecules in the asymmetric unit, which is different from the crystals of Padron0.9 (PDB entry 3lsa; Brakemann *et al.*, 2010). As demonstrated previously, despite being monomeric in solution, Padron0.9 forms tetramers within the crystal. The tetramers of Padron0.9 are comparable to the naturally occurring RSFP (asFP595) from *Anemonia sulcata*, which is biologically a tetramer (Nienhaus *et al.*, 2006). In the case of Tetdron, at equilibrium, the room-temperature X-ray structure does not reveal tetramers forming within the crystal, but rather its molecules are aligned along the crystallographic *b* axis. The difference in the crystal packing between Padron0.9 and Tetdron may be attributed to the difference in the amino-acid sequence at the N-termini, crystallization conditions, and acid-base equilibrium properties of the chromophore discussed below.

The room-temperature X-ray structure of Tetdron was obtained at a resolution of 2.05 Å (see Table 1 for the data-collection and refinement statistics). The overall structure of a protein monomer is practically unchanged compared with the cryogenic X-ray structure of Padron0.9, with an RMSD of 0.155 Å when the Cα atoms are aligned [Fig. 2(*a*)]. Specifically, in the equilibrium state of Tetdron the chromophore is in the *trans* configuration [see Fig. 2(*c*) and Supplementary Fig. S1 in the Supporting information] similar to that for the Padron0.9 non-fluorescent 'off' state. Moreover, no conformational changes are present for the residues near the chromophore when the two structures are compared [Fig. 2(*b*)]. Within the β-barrel of Tetdron, the *p*-hydroxyphenyl group of the chromophore is hydrogen bonded to Y159 and a structural water molecule, which in turn is hydrogen bonded to T175 [Fig. 2(*b*)]. These hydrogen bonds drive the *cis*–*trans* equilibrium of the chromophore towards the *trans* configuration. Therefore, Y159 and the structural water molecule can be involved in the proton transfer during photo-switching because they form direct hydrogen bonds to the *p*-hydroxyphenyl group. Near the chromophore, there is an extended hydrogen-bonding network comprising residues E144, H193 and E211, which may also influence the pK_a and the ESPT from the *p*-hydroxyphenyl group during the photo-switching process.

In addition to the hydrogenated protein crystal of Tetdron, we obtained a room-temperature X-ray structure of the deuterated Tetdron at a resolution of 1.90 Å (Table 1). The rationale was to detect possible heavy protein-isotope effects on its photo-physical properties and to conduct neutron-crystallography experiments in the future to directly and fully map the positions of hydrogen atoms in this RSFP. No significant differences are apparent both globally and around the chromophore when comparing the crystal structures of the hydrogenated and deuterated Tetdron [Figs. 3(*a*)–3(*c*) and Supplementary Fig. S2]. To switch Tetdron fully to the non-fluorescent 'off' state of the chromophore, a deuterated crystal was illuminated with 400 nm light at room temperature for about 4 min using a 150 W UV lamp. The room-temperature X-ray crystal structure of the 400 nm irradiated state was

obtained at a resolution of 2.4 Å (Table 1). Interestingly, no structural changes near the chromophore were observed when comparing the equilibrium structure with that of the 400 nm irradiated crystal [Figs. 3(*d*)–3(*f*)]. However, quite remarkably and unexpectedly, large-scale changes of the unit-cell dimensions and the crystal packing (Fig. 4) were detected (Table 1). Specifically, the unit-cell edges *a*, *b* and *c* increase by *ca* 2%, 7% and 17%, respectively, while the crystal remains intact and the space group does not change. Additionally, examination of the new crystal packing reveals that the 400 nm irradiation causes substantial shifts in protein-molecule positions, leading to the apparent tetramerization of Tetdron *in crystallo* without destroying the crystal (Fig. 4). Thus, the UV light has triggered a martensitic transformation – a first-order single-crystal-to-single-crystal phase transition – in a Tetdron crystal. The tetrameric arrangement formed within the illuminated crystal has the same organization as in the crystals of Padron0.9 and asFP595 (Brakemann *et al.*, 2010; Andresen *et al.*, 2005), both of which contain essentially fully deprotonated chromophore in their equilibrium states (Supplementary Fig. S3). Also, the chromophore in Tetdron remains in the *trans* configuration. Such a large rearrangement of Tetdron molecules within the crystal upon irradiation can only occur if the protein molecules become much more dynamic after absorbing a photon of light, but before they fully return to the low-energy vibrational levels on the ground-state free-energy surface. The new tetrameric form of Tetdron remains stable in the crystal, as the unit-cell dimensions do not change over a period of months, even though the UV–vis spectra slowly transition back towards the initial equilibrium-state spectra as discussed below.

Table 1
Room-temperature X-ray data-collection and refinement statistics.

	Hydrogenated Tetdron at equilibrium 6mxw	Deuterated Tetdron at equilibrium 6myb	400 nm irradiated deuterated Tetdron 6myc
Data collection			
Beamline/facility	Rigaku Home Source	LS-CAT 21-F APS	Rigaku Home Source
Resolution range (Å)	40.0–2.05 (2.12–2.05)	40.0–1.9 (1.97–1.90)	40.00–2.4 (2.48–2.40)
Space group	$P2_1$	$P2_1$	$P2_1$
Unit-cell parameters (Å, °)	a = 71.7, b = 129.9, c = 98.7, β = 105.3	a = 71.6, b = 129.6, c = 98.6, β = 105.3	a = 73.0, b = 138.1, c = 115.8, β = 104.5
Unique reflections	52462 (4211)	42320 (4552)	30436 (3182)
Redundancy	2.9 (2.4)	3.0 (2.8)	2.9 (2.8)
Completeness (%)	96.0 (92.6)	93.2 (94.0)	89.5 (90.7)
Mean $I/\sigma(I)$	74.0 (2.5)	8.9 (2.5)	42.6 (1.4)
R_{merge}	0.043 (0.344)	0.10 (0.388)	0.049 (0.63)
Refinement			
R_{work}	0.157 (0.160)	0.199 (0.238)	0.153 (0.343)
R_{free}	0.202 (0.202)	0.250 (0.294)	0.211 (0.379)
No. of non-hydrogen atoms	14564	14675	14076
Macromolecules	13886	13886	13810
Water	739	815	262
RMS (bonds)	0.007	0.007	0.008
RMS (angles)	1.01	0.99	1.08
Ramachandran plot			
Favored (%)	98.88	98.99	97.38
Allowed (%)	0.95	0.95	2.33
Outliers (%)	0.18	0.06	0.18
Clashscore	2.72	3.67	6.11
Average B factor (Å^2)	29.3	22.9	46.5
Macromolecules	29.1	22.8	46.7
Solvent	31.8	26.0	37.7

2.2. Photo-induced deprotonated *trans*-chromophore is a long-lived state in solution and in crystals

In solution, at equilibrium, the UV–vis absorption spectra of Tetdron indicate that there is a mixture of protonated and deprotonated forms of the chromophore [Fig. 2(*d*)]. Two absorption bands, at 400 nm and 500 nm, are observed representing populations of the protonated (neutral) and deprotonated (anionic) states of the chromophore's *p*-hydroxyphenyl group, respectively. Upon irradiation with 400 nm light, the 400 nm band intensity decreases to essentially zero, thus shifting Tetdron to a fully deprotonated non-fluorescent 'off' state [Fig. 2(*d*)], while keeping the chromophore in the *trans* configuration as shown by our room-temperature X-ray structure. The calculated molar extinction coefficients (ε) for the deprotonated and protonated chromophores are 50 000 and 33 000 M^{-1} cm^{-1}, respectively. These values were obtained based on the height of the 500 nm absorption band in the 400 nm irradiated, fully deprotonated, Tetdron sample and on the protein concentration (obtained through the quantitative net peptide analysis; see *Methods*) using the standard Beer–Lambert law. Thus, at equilibrium, we estimate that there is an ∼1:1 mixture of the protonated-to-deprotonated chromophore states, suggesting that the apparent pK_a of the *p*-hydroxyphenyl group is ∼7, despite the fact that, based on the structure, the *p*-hydroxyphenyl group appears to be shielded from the bulk solvent. This Tetdron property distinguishes it from Padron and Padron0.9, which contain mostly deprotonated chromophores in their respective equilibrium states (Brakemann *et al.*, 2010; Regis Faro *et al.*, 2011). When the 'off' state of Tetdron is irradiated with 532 nm light, re-protonation of the *p*-hydroxyphenyl group occurs, as indicated by the re-emergence and the height of the 400 nm band [Fig. 2(*d*)]. Based on the studies of Padron and Padron0.9, the chromophore re-protonation in Tetdron must similarly be accompanied by the *trans*-to-*cis* isomerization around the C=C double bond in the *exo*-position of the imidazolinone ring.

As stated above, irradiating the equilibrium state of Tetdron with 400 nm light excites the protonated form of the chromophore into an electronically excited state, followed by the ESPT to result in a fully deprotonated chromophore population. Interestingly, the recovery back to equilibrium (Fig. 5) takes ∼9 days in solution, suggesting that the chromophore's proton is moved to the bulk solvent during ESPT, and the

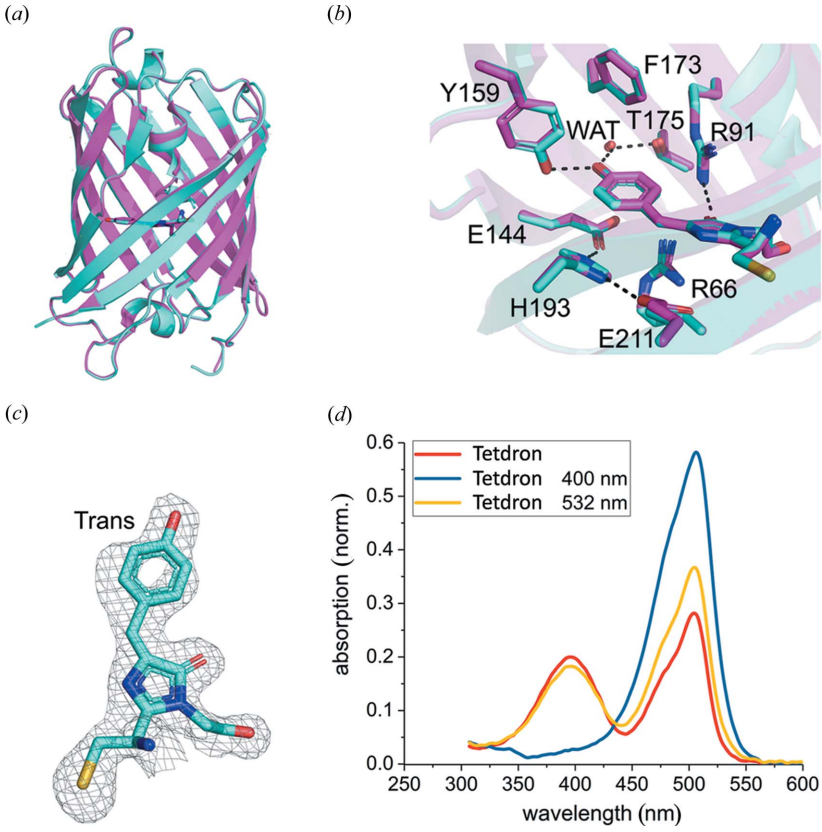

Figure 2
(*a*) Structure of the hydrogenated Tetdron monomer (cyan) at equilibrium aligned with Padron0.9 'off-state' (magenta). (*b*) Structural alignment close-up of the chromophore site with surrounding residues of Tetdron (cyan) and Padron0.9 (magenta). (*c*) Electron-density map for the chromophore refined with 100% occupancy in the *trans* configuration for hydrogenated Tetdron at equilibrium (also see Supplementary Fig. S1). The grey mesh is a $2|F_o|-|F_c|$ electron-density map contoured at 1σ. (*d*) Solution UV–vis absorption spectra of Tetdron before (red line) and after (blue–grey and yellow lines) irradiation. The blue–grey spectrum was recorded after 400 nm irradiation, followed by 532 nm irradiation resulting in the yellow spectrum.

energy barrier for the ground-state proton transfer in the reverse direction is relatively high. Thus, the proton-transfer events in Tetdron must be rather complex, probably involving protein conformational dynamics coupled to the bulk solvent. Moreover, the rate of the ground-state proton transfer in the reverse reaction within the crystal of Tetdron is even smaller (>18 days) compared with that in solution (Supplementary Fig. S4). Therefore, the restricted motions of the protein in the crystal lattice further inhibit the recovery back to the equilibrium, suggesting that protein dynamics and, perhaps, local unfolding in Tetdron assist in the ground-state and excited-state proton-transfer events.

When Tetdron is deuterated, there is a visual difference in the protein-solution colour compared with the hydrogenated protein. Deuterated Tetdron solution appears slightly more orange [Fig. 6(*a*)]. However, there is a negligible increase in the 500 nm band, but a more significant decrease in the 400 nm band with respect to the UV–vis absorption spectra for hydrogenated Tetdron. Also, the same trend is observed when comparing UV–vis absorption spectra of the hydrogenated and deuterated crystals of the protein [Fig. 6(*b*)]. Yet, we calculate that deuterated Tetdron still exhibits an ∼1:1 ratio of the protonated-to-deprotonated chromophore states, suggesting that deuteration does not alter the pK_a of the *p*-hydroxyphenyl group, only changing the extinction coefficients for the absorption bands. To further validate that deuteration does not alter the acid-base equilibrium of the chromophore, we obtained UV–vis spectra at low pH [Fig. 6(*c*)]. At pH 5.3, the 400 nm band increases while the 500 nm decreases with comparable magnitude for the deuterated and hydrogenated Tetdron, providing further evidence that deuteration does not alter the chromophore's pK_a. Rather, previous studies of the heavy protein-isotope effects in FPs showed increased fluorescence lifetimes associated with the deprotonation of the chromophore (Bae *et al.*, 2003). Indeed, we found that the visual and spectroscopic differences between the deuterated and hydrogenated Tetdron are caused by changes in the molar extinction coefficients (ε) for the protonated (neutral) chromophore in the deuterated Tetdron compared with its hydrogenated protein. The molar extinction coefficients for the deprotonated and protonated chromophores are 50 000 and 22 000 M^{-1} cm^{-1}, respectively, for the deuterated protein. Therefore, there is an 11 000 M^{-1} cm^{-1} reduction in extinction for the protonated chromophore in the deuterated Tetdron, which is likely to be caused by changes in the vibronic coupling and the transition dipoles caused by the heavier mass of deuterium.

2.3. Fluorescence mapping provides evidence of heavy protein-isotope effects

To study the effects of crystal packing on fluorescence and obtain a more detailed picture of Tetdron fluorescence properties, we conducted fluorescence-mapping experiments for hydrogenated and deuterated Tetdron samples both in solution and in single crystals (Fig. 7 and Supplementary Fig. S5). These experiments were performed with the excitation light in the 300–550 nm range, while monitoring fluorescence in the 300–700 nm range. Importantly, solution and single-crystal fluorescence-mapping experiments were conducted on the non-irradiated samples at equilibrium containing a 1:1 mixture of protonated and deprotonated chromophores in the *trans* configuration; their UV–vis spectra remained identical to those collected prior to the fluorescence-mapping experiments. Overall, in solution, hydrogenated and deuterated Tetdron fluoresce at around 525 nm irrespective of the excitation-light wavelength, indicating that only the deprotonated chromophore is emitting light even when Tetdron is excited into the protonated-chromophore absorption band at 400 nm. When the excitation-light wavelength is below ∼450 nm the

fluorescence is moderate but increases significantly in intensity when the sample is excited with light in the 470–500 nm range. Hydrogenated Tetdron has marginally stronger overall fluorescence than the deuterated protein when excited with UV light [Figs. 7(*a*) and 7(*b*), and Supplementary Fig. S5], which is probably because of the higher molar extinction coefficient for the protonated chromophore in the former. Therefore, in solution, the 300–450 nm light excites the protonated form of the chromophore, followed by the ESPT, allowing the deprotonated chromophore in the *trans* configuration to emit light at a wavelength of ∼525 nm. This is because the UV light does not trigger *trans–cis* isomerization in Tetdron as demonstrated by our photo-crystallographic experiments. When the sample is excited with the 500 nm light, we cannot rule out the possibility that some chromophores can undergo *trans–cis* isomerization, but the quantum yield of this structural rearrangement is probably lower than 100%. Interestingly, negligible fluorescence at 525 nm is observed when the hydrogenated or deuterated Tetdron single crystals are excited with UV light between 300 and 450 nm [Figs. 7(*c*) and 7(*d*), and Supplementary Fig. S5]. Rather, emission is observed at 425 nm from a deuterated crystal when excited with 375 nm light [Fig. 7(*d*)], suggesting that direct fluorescence of the protonated *trans* chromophore can be induced within

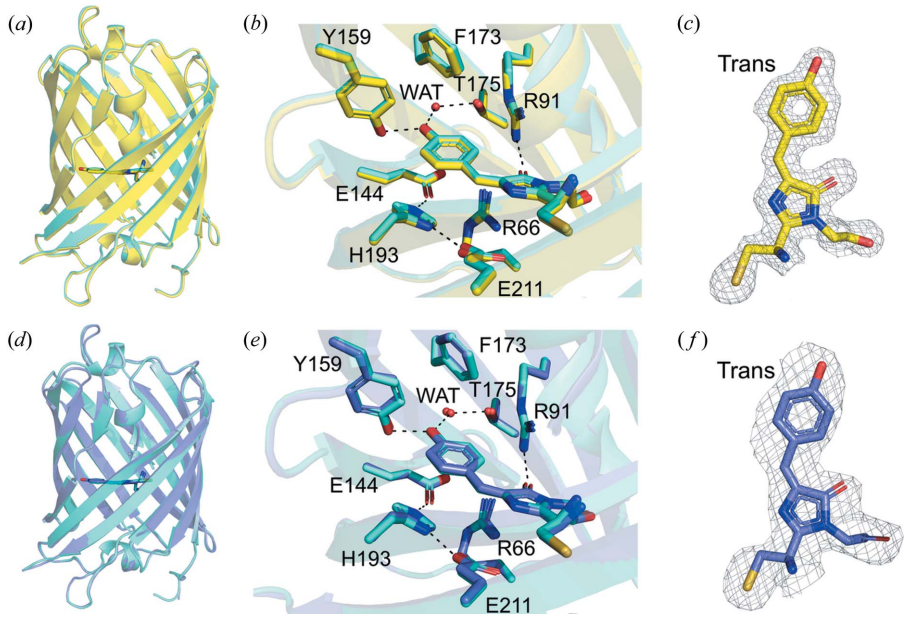

Figure 3
Structure of deuterated Tetdron in the equilibrium state (*a*–*c*) and deuterated Tetdron in the 'off-state' after 400 nm irradiation (*d*–*f*). (*a*) Structural alignment of deuterated (yellow) and hydrogenated (cyan) Tetdron at equilibrium. (*b*) Structural alignment close-up of the chromophore site with surrounding residues. (*c*) Electron density of the chromophore in the *trans* configuration for deuterated Tetdron at equilibrium. The grey mesh is a $2|F_o|-|F_c|$ electron-density map contoured at 1σ. (*d*) Structural alignment of deuterated Tetdron after 400 nm irradiation ('off-state', purple), and hydrogenated Tetdron at equilibrium (cyan). (*e*) Structural alignment close-up of the chromophore site with surrounding residues. (*f*) Electron density of the chromophore in the *trans* configuration for deuterated Tetdron after 400 nm irradiation. The grey mesh is a $2|F_o|-|F_c|$ electron-density map contoured at 1σ.

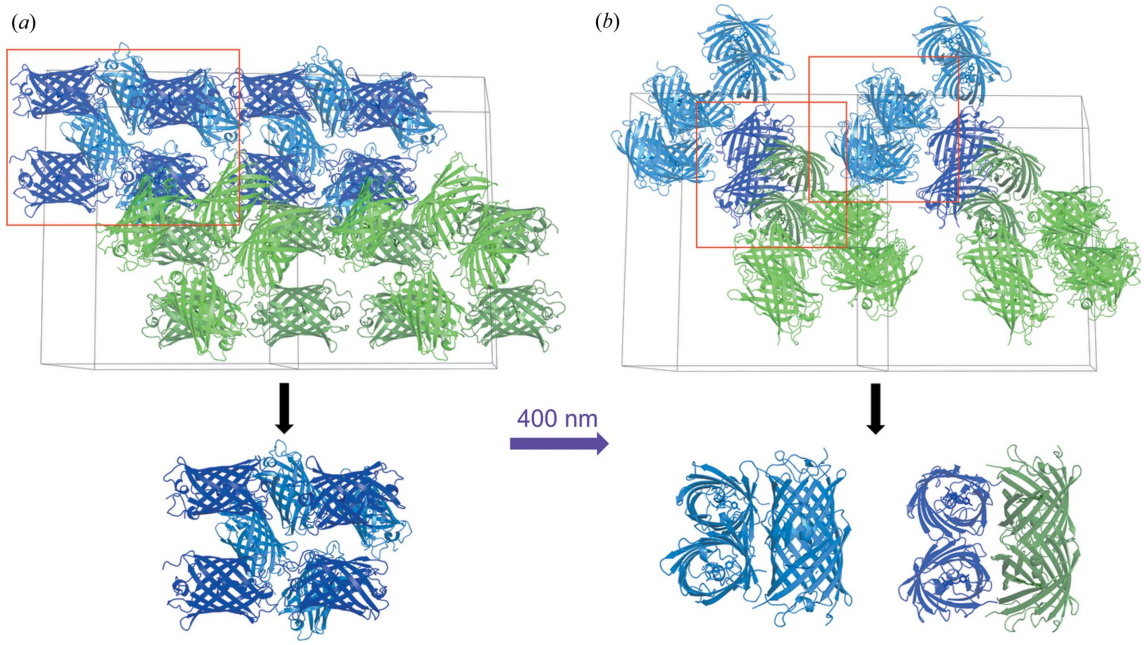

Figure 4
Crystal packing in Tetdron showing a super cell along the *b* axis. (*a*) Tetdron in the equilibrium state with a single asymmetric unit below. (*b*) Tetramers of the 400 nm irradiated Tetdron that form within the same asymmetric unit (blue) and within a neighbouring asymmetric unit (blue and green). Red boxes indicate the molecules that were used to generate the images shown immediately under the super cells.

the crystal of the heavy protein. The 425 nm fluorescence band is significantly weaker for the hydrogenated crystal, indicating that deuteration reduces the non-radiative decay.

3. Discussion

It was unexpected to discover that Tetdron contains a mixture of protonated and deprotonated forms of the chromophore [Fig. 2(*d*)] at equilibrium with a 1:1 ratio giving it unique properties that neither Padron nor Padron0.9 possess. Interestingly, L141P substitution in Padron0.9 results in a similar mixture of the protonated and deprotonated forms of the chromophore at equilibrium for this variant, but no photo-physical or structural analyses have been conducted for Padron0.9 L141P (Brakemann *et al.*, 2010). Tetdron exhibits similar photo-chromic and photo-switching properties to Padron and Padron0.9, as indicated by the UV–vis spectra [Fig. 2(*d*)]. More specifically, the 400 nm and 500 nm absorption bands correspond to the protonated and deprotonated *p*-hydroxyphenyl group of the chromophore, respectively. When Tetdron is irradiated with 400 nm light to excite the protonated form, that induces ESPT to give a long-lived fully deprotonated species [Fig. 2(*d*)], followed by fluorescence from the anionic chromophore (Fig. 7). If there is no population of the protonated chromophore, as is the case in the equilibrium states of Padron and Padron0.9, 400 nm light would not excite the chromophore. Moreover, when Padron and Padron0.9 are irradiated with 500 nm light to excite the deprotonated chromophore, that results in a *trans*-to-*cis* isomerization, fluorescence from the anionic chromophore and re-protonation of a portion of chromophores in the *cis* configuration (Brakemann *et al.*, 2010; Regis Faro *et al.*, 2011), and these photo-physical and photo-chemical properties should be the same for Tetdron.

What distinguishes Tetdron from its parent proteins Padron and Padron0.9, and to the best of our knowledge from all other proteins, is the fact that the 400 nm light irradiation into the protonated-chromophore absorption band in the crystal causes dramatic rearrangement of the crystal packing, resulting in a first-order crystal-to-crystal phase transition called a martensitic transformation. Based on our room-temperature X-ray crystal structures of Tetdron before and after irradiation, it is evident that the protein molecules shift within the crystal lattice upon light absorption. The 400 nm light induces deprotonation of virtually all chromophores leading the irradiated Tetdron molecules, which now contain

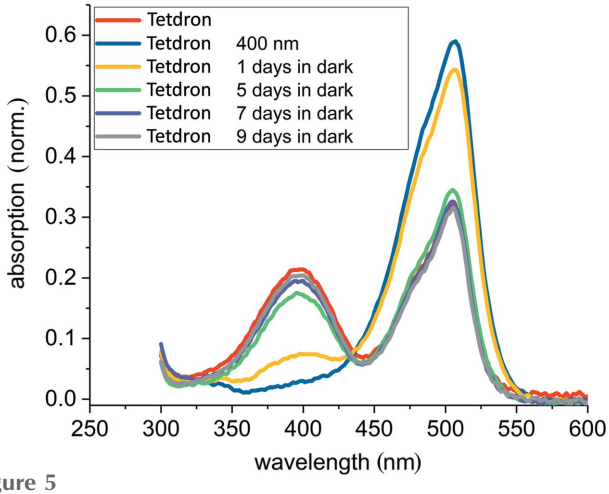

Figure 5
Solution UV–vis spectra of Tetdron before (red) and after (blue) irradiation with 400 nm light, followed by relaxation and re-protonation of the chromophore in the dark (yellow to grey lines).

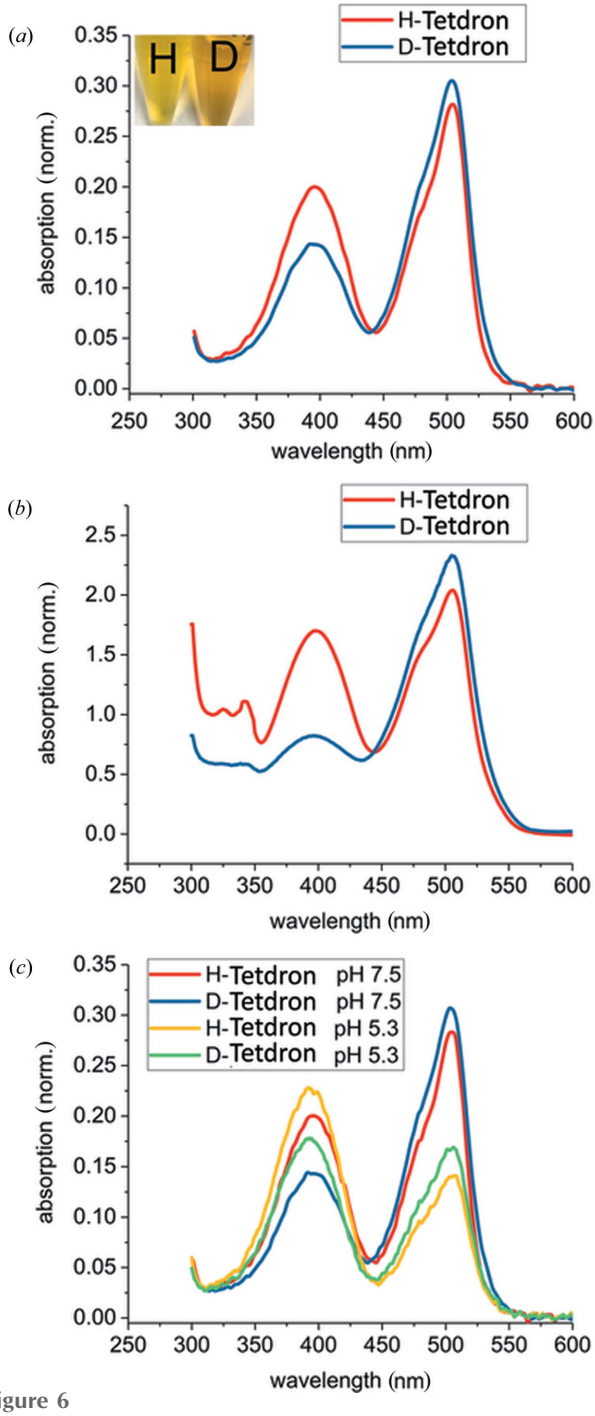

Figure 6
UV–vis spectra of hydrogenated and deuterated Tetdron in (*a*) solution and in (*b*) the crystal. (*c*) Comparison of solution UV–vis spectra at neutral and low pHs.

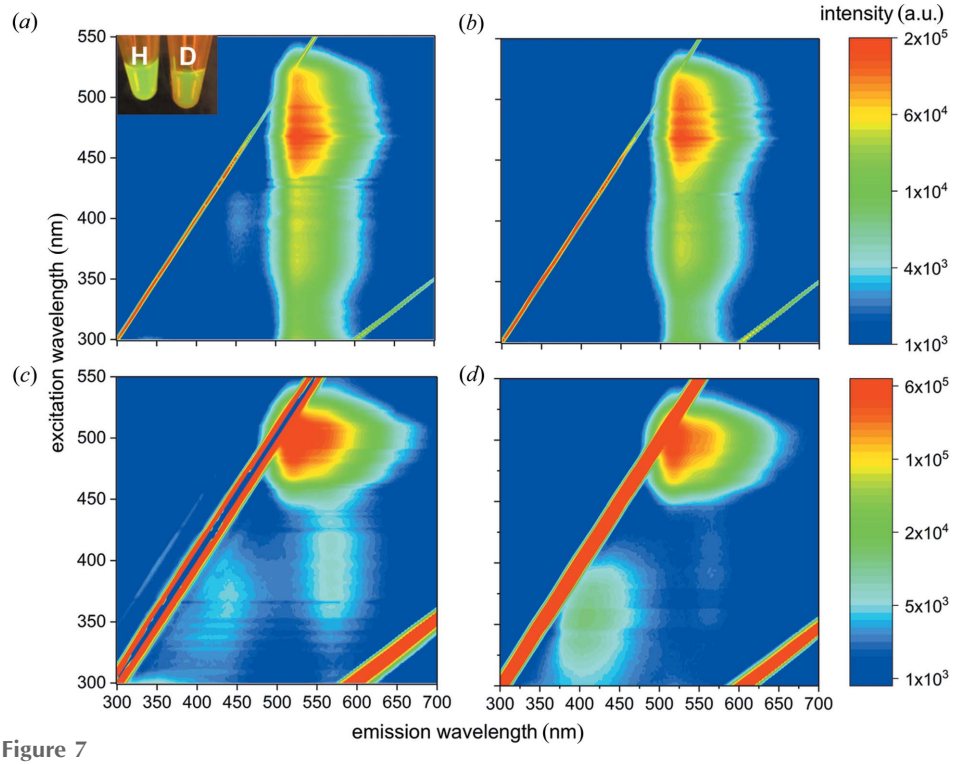

Figure 7
Fluorescence mapping of Tetdron. Solution measurements of (*a*) hydrogenated and (*b*) deuterated Tetdron. Crystal measurements of (*c*) hydrogenated and (*d*) deuterated Tetdron.

only anionic chromophores, to tetramerize *in crystallo* (Fig. 4). Thus, Tetdron tetramerization is driven by the deprotonation and ionization of the chromophores within the protein molecules. Changes in protonation states of the surface residues during this process can also occur, but they can only be directly visualized by neutron crystallography.

The fact that during the photo-induced martensitic transformation of Tetdron crystals the long-range crystalline order remains intact is completely unexpected because (1) protein movement should be greatly restricted in a crystal and (2) significant molecular movement usually destroys the crystal. It is possible that, after the chromophore is deprotonated in the excited state, the protein dynamics allow Tetdron molecules to move more freely and tetramerize, resulting in the observed crystal-to-crystal phase transition. If, however, the sequence of events is similar to that reported for Dronpa (Warren *et al.*, 2013), a competing mechanism would involve the protonated chromophore in the electronically excited state crossing over to a vibrationally hot ground state through the internal conversion. In this high-energy ground state, large collective protein motions would allow the bulk solvent to reach and deprotonate the chromophore, with the molecules subsequently returning to a low-energy vibrational level through non-radiative decay. In any of the two above scenarios, once the chromophore is deprotonated, the equilibrium shifts towards tetramerization of the anionic Tetdron molecules, which ultimately relax to the new stable crystal lattice. This process gives identical tetramers to those of asFP595 protein at equilibrium (Supplementary Fig. S3). Our experiments cannot distinguish between these two competing hypotheses, but both, the excited-state and ground-state proton-transfer events followed by tetramerization, can play out in the case of Tetdron. The martensitic transformation that leads to the tetramerization of Tetdron *in crystallo* appears to be an irreversible transition, similar to that observed in steels, because the new crystal form does not revert to the equilibrium crystal form after the chromophores are spontaneously protonated over the period of several weeks following irradiation. When comparing spectroscopic measurements in solution with those in the crystals [Figs. 2(*d*) and 5], it is evident that the crystal packing inhibits the ground-state proton transfer in the direction of re-protonating the chromophores after 400 nm irradiation, because protein motions are hindered in the crystal lattice as it takes on the order of weeks longer in the Tetdron crystal than in solution for the UV–vis spectra to recover (Fig. 5 and Supplementary Fig. S4). Because of the complexity of the protein matrix, the role of dynamics in RSFPs has been poorly understood and only recently has gained attention because of development of more robust computer simulations and time-resolved experiments (Demachy *et al.*, 2005; Ding *et al.*, 2013; Coquelle *et al.*, 2018).

Over the years RSFPs have played key roles in the development of nanoscopy and fluorescence imaging to peer deep into the cell function. Recently, two newer potential applications for RSFPs (and for other protein molecules) have emerged – optogenetics and high-density optical data storage. In optogenetics, light-induced association (multimerization) and/or dissociation of protein molecules is essential to control the functions of other proteins, such as enzymes (Zhou *et al.*, 2012; Nihongaki *et al.*, 2014; Cambridge, 2014). Optically controlled multimerization of the same protein molecules, so-called homomultimerization, is a preferred property that a candidate molecule should possess. In this regard Tetdron appears to be well suited as a potential candidate for optogenetic applications, and its light-induced homotetramerization capability can be further explored. Additionally, the ability of Tetdron to tetramerize in the solid state after light illumination without destroying the crystal lattice can be of great utility for its potential application in optical data storage. RSFPs have shown great potential for creating next-generation ultrahigh-density optical data-storage devices (Grotjohann *et al.*, 2011; Adam *et al.*, 2010). Single crystals of these proteins have been proposed as 3D data-storage media, in which, theoretically, each protein molecule would represent a data bit. But, in practice, it is not possible to address an

individual RSFP molecule, which is roughly 5 nm in size, within a dense crystalline environment with current laser technology. However, it is now possible to perform diffraction-unlimited all-optical imaging at resolutions of several tens of nanometres. The unit-cell dimensions for Tetdron crystals are ∼10 nm, which might still be too small. But, if each individual unit cell in a Tetdron crystal could be illuminated and the protein molecules within it converted to non-fluorescent tetramers without inducing changes in the adjacent unit cells, then each unit cell can represent a data bit. In this hypothetical data-writing scheme, sixteen Tetdron molecules would need to be illuminated, instead of only one, which may be substantially less technically complicated. For example, a 1 mm^3 crystal of Tetdron contains about 10^{15} unit cells; thus, in theory, about 1 petabit of data can be written in, which would represent an enormous amount of information held in such a tiny volume. Although long-term data storage based on protein crystals may be problematic because of stability issues, they may be useful in situations where biodegradability and quick destruction are desirable, such as in storing digital soft keys and passwords for national security.

Finally, the remarkable and unique property of Tetdron crystals to undergo a photo-induced martensitic transformation can be explored to create novel martensitic biomaterials. One area of interest is to make materials-as-machines for biomedical applications (Bhattacharya & James, 2005), in which a protein molecule would play the role of a tiny molecular nanomachine to produce work, just like the bacteriophage T4 tail sheath transformation that leads to puncturing of a tough bacterial cell wall by a specialized viral protein needle. The fact that the martensitic transformation of Tetdron is triggered by light may be used in future molecular nanomachines that would operate under 'light on'/'light off' stimuli.

4. Methods

4.1. Protein expression, purification and crystallization

The *Escherichia coli* codon-optimized gene for Tetdron, with an N-terminal His-tag and a tobacco etch virus (TEV) protease cleavage site, was synthesized based on the Padron0.9 sequence (PDB entry 3lsa) and cloned into the pJ411 vector, purchased from ATUM (Newark, California, USA). For the deuterated protein expression of Tetdron, *E. coli* BL21(DE3) cells containing the Tetdron plasmid were grown in minimal medium with 99.8% D_2O and hydrogenous glycerol as the carbon source to give ∼80% incorporation of deuterium. A bioreactor (BIOFLO 310, Eppendorf) was used for protein expression to obtain high quantities of the deuterated protein. The cells were grown to an OD_{600} of 10.0 at 30°C, induced at 20°C with 1 m*M* isopropyl *β*-D-thiogalactopyranoside and fed with hydrogenous glycerol solution in D_2O for 24 h. The cell paste was stored at −80°C until needed for protein purification. For hydrogenated protein expression, the shake-flask method was used with Luria–Bertani broth as the growth medium. The induced cells were resuspended in 5 ml of lysis buffer (50 m*M* sodium phosphate pH 7.5, 250 m*M* NaCl and 10 m*M* imidazole) per gram of cells and then lysed by sonication. Lysates, clarified by centrifugation, were loaded onto a 10 ml Ni–Sepharose column (Sepharose 6 Fast Flow, GE Healthcare) equilibrated with buffer A (50 m*M* sodium phosphate pH 7.5, 500 m*M* NaCl and 10 m*M* imidazole). Tetdron was eluted by using a 50 ml linear gradient to 100% Buffer B (50 m*M* sodium phosphate pH 7.5, 500 m*M* NaCl, and 500 m*M* imidazole). The eluted fractions were collected, pooled, and 1 mg of TEV protease per 100 mg of target protein was added and dialyzed overnight in buffer (50 m*M* Tris–HCl pH 7.5, 0.1 m*M* EDTA and 1 m*M* DTT). The dialyzed protein fractions were subsequently loaded onto a second 10 ml Ni–Sepharose 6 column, and the flow-through containing tagless Tetdron was collected. The purified Tetdron was buffer exchanged by dialysis into 50 m*M* Tris pH 7.5 and 0.15 *M* NaOAc, concentrated to ∼24 mg ml^{-1} (Amicon Ultra 10 K), and crystallized by sitting-drop vapour diffusion using a 1:1 ratio of protein to crystallization solution [50 m*M* Tris pH 7.5, 0.15 *M* NaOAc, and 24% (*w*/*v*) polyethylene glycol 4000] in Hampton sandwich boxes (Hampton Research, Aliso Viejo, California, USA).

4.2. X-ray diffraction data collection, processing and refinement

The room-temperature X-ray data for Tetdron crystals were collected using a Rigaku HighFlux HomeLab instrument equipped with a MicroMax-007 HF X-ray generator, Osmic VariMax optics and an R-AXIS IV^{++} image-plate detector, or at the LS-CAT ID-G (APS, ANL) using a Dectris EIGER 9M detector. For the 400 nm irradiated X-ray structure, prior to data collection, one crystal was irradiated for 4 min with an OPTI-LUX 400 UV 150 W lamp, switching Tetdron to a completely deprotonated state of the chromophore. For all data sets, the *HKL*3000 software suite (Minor *et al.*, 2006) was utilized for the diffraction data integration and scaling. Tetdron crystallized in a monoclinic space group ($P2_1$). The structure was solved using molecular replacement and PDB entry 3lsa as a search model (*Phaser*, *CCP4*; McCoy *et al.*, 2007; Winn *et al.*, 2011). Following phasing, several rounds of *XYZ* coordinate, real-space, occupancy, and *B*-factor refinement were carried out using *phenix.refine* (Adams *et al.*, 2002; Afonine *et al.*, 2012). Between each round of refinement, the program *Coot* was used to manually adjust the Tetdron models (Emsley & Cowtan, 2004). The crystallographic data-collection and refinement statistics are given in Table 1.

4.3. UV–vis and fluorescence spectroscopy

For the solution spectroscopic measurements, the concentration of the protein was initially determined by 280 nm absorbance using a NanoDrop 2000, where the extinction coefficient for the protein was predicted by the ExPASy online server (https://web.expasy.org/protparam). For further validation of the protein concentration, both hydrogenated and deuterated protein samples were sent to New England Peptide for amino-acid analysis. It is important to note that for the

solution-spectroscopy experiments the same concentration of hydrogenated and deuterated Tetdron were used for each measurement. Specifically, for the solution UV–vis measurements, the UV-2700 Shimadzu UV–vis spectrophotometer and the NanoDrop 2000 instruments were used. For both crystal UV–vis and fluorescence measurements, a Tetdron crystal was mounted in a rectangular quartz capillary. The *in crystallo* UV–vis spectroscopy was conducted on the Cary 5000 spectrophotometer using a sample holder that was machined in-house with a 1 mm pin hole. Steady-state fluorescence of solutions and crystals was measured using a dual grating Fluorolog 3T (JY Horiba) in a right-angle configuration of excitation emission. Fluorescence mapping was used to optimize the excitation wavelength of emission, and a 5.0 second integration time was used.

Funding information

This research used resources of the Advanced Photon Source, a US Department of Energy (DOE) Office of Science User Facility operated for the DOE Office of Science by Argonne National Laboratory under Contract No. DE-AC02-06CH11357. The D_2O used in this research was supplied by the United States Department of Energy Office of Science by the Isotope Program in the Office of Nuclear Physics. The Office of Biological and Environmental Research supported research at Oak Ridge National Laboratory's (ORNL) Center for Structural Molecular Biology (CSMB) involving protein deuteration, using facilities supported by the Scientific User Facilities Division, Office of Basic Energy Sciences, US Department of Energy. Optical measurements were conducted at the ORNL Center for Nanophase Materials Sciences (CNMS) supported by the Scientific User Facilities Division, Office of Basic Energy Sciences, US Department of Energy. This manuscript has been authored by UT-Battelle LLC under DOE Contract No. DE-AC05-00OR22725.

References

Adam, V., Lelimousin, M., Boehme, S., Desfonds, G., Nienhaus, K., Field, M. J., Wiedenmann, J., McSweeney, S., Nienhaus, G. U. & Bourgeois, D. (2008). *Proc. Natl Acad. Sci. USA*, **105**, 18343–18348.

Adam, V., Mizuno, H., Grichine, A., Hotta, J.-I., Yamagata, Y., Moeyaert, B., Nienhaus, G. U., Miyawaki, A., Bourgeois, D. & Hofkens, J. (2010). *J. Biotechnol.* **149**, 289–298.

Adams, P. D., Grosse-Kunstleve, R. W., Hung, L.-W., Ioerger, T. R., McCoy, A. J., Moriarty, N. W., Read, R. J., Sacchettini, J. C., Sauter, N. K. & Terwilliger, T. C. (2002). *Acta Cryst.* D**58**, 1948–1954.

Afonine, P. V., Grosse-Kunstleve, R. W., Echols, N., Headd, J. J., Moriarty, N. W., Mustyakimov, M., Terwilliger, T. C., Urzhumtsev, A., Zwart, P. H. & Adams, P. D. (2012). *Acta Cryst.* D**68**, 352–367.

Ando, R., Mizuno, H. & Miyawaki, A. (2004). *Science*, **306**, 1370–1373.

Andresen, M., Stiel, A. C., Fölling, J., Wenzel, D., Schönle, A., Egner, A., Eggeling, C., Hell, S. W. & Jakobs, S. (2008). *Nat. Biotechnol.* **26**, 1035–1040.

Andresen, M., Stiel, A. C., Trowitzsch, S., Weber, G., Eggeling, C., Wahl, M. C., Hell, S. W. & Jakobs, S. (2007). *Proc. Natl Acad. Sci. USA*, **104**, 13005–13009.

Andresen, M., Wahl, M. C., Stiel, A. C., Gräter, F., Schäfer, L. V., Trowitzsch, S., Weber, G., Eggeling, C., Grubmüller, H. & Hell, S. W. (2005). *Proc. Natl. Acad. Sci. USA*, **102**, 13070–13074.

Anwar, J., Tuble, S. C. & Kendrick, J. (2007). *J. Am. Chem. Soc.* **129**, 2542–2547.

Bae, J. H., Rubini, M., Jung, G., Wiegand, G., Seifert, M. H., Azim, M. K., Kim, J.-S., Zumbusch, A., Holak, T. A., Moroder, L., Huber, R. & Budisa, N. (2003). *J. Mol. Biol.* **328**, 1071–1081.

Bhattacharya, K. & James, R. D. (2005). *Science*, **307**, 53–54.

Brakemann, T., Weber, G., Andresen, M., Groenhof, G., Stiel, A. C., Trowitzsch, S., Eggeling, C., Grubmüller, H., Hell, S. W. & Wahl, M. C. (2010). *J. Biol. Chem.* **285**, 14603–14609.

Cambridge, S. (2014). Editor. *Photoswitching Proteins: Methods and Protocols*, Vol. 1148, *Methods in Molecular Biology*. New York: Humana Press.

Campbell, B. C., Petsko, G. A. & Liu, C. F. (2018). *Structure*, **26**, 225–237.e3.

Chang, H., Zhang, M., Ji, W., Chen, J., Zhang, Y., Liu, B., Lu, J., Zhang, J., Xu, P. & Xu, T. (2012). *Proc. Natl Acad. Sci. USA*, **109**, 4455–4460.

Christian, J. W. (2002). *The Theory of Transformations in Metals and Alloys*, 3rd ed. Oxford: Pergamon Press.

Coquelle, N., Sliwa, M., Woodhouse, J., Schirò, G., Adam, V., Aquila, A., Barends, T. R., Boutet, S., Byrdin, M. & Carbajo, S.(2018). *Nat. Chem.* **10**, 31–37.

Demachy, I., Ridard, J., Laguitton-Pasquier, H., Durnerin, E., Vallverdu, G., Archirel, P. & Lévy, B. (2005). *J. Phys. Chem. B*, **109**, 24121–24133.

Ding, L., Chung, L. W. & Morokuma, K. (2013). *J. Phys. Chem. B*, **117**, 1075–1084.

Duan, C., Adam, V., Byrdin, M. & Bourgeois, D. (2014). *Photoswitching Proteins: Methods and Protocols*, Vol 1148, *Methods in Molecular Biology*, pp. 177–202. New York: Humana Press.

Emsley, P. & Cowtan, K. (2004). *Acta Cryst.* D**60**, 2126–2132.

Falk, W. & James, R. D. (2006). *Phys. Rev. E*, **73**, 011917.

Grotjohann, T., Testa, I., Leutenegger, M., Bock, H., Urban, N. T., Lavoie-Cardinal, F., Willig, K. I., Eggeling, C., Jakobs, S. & Hell, S. W. (2011). *Nature*, **478**, 204–208.

Habuchi, S., Ando, R., Dedecker, P., Verheijen, W., Mizuno, H., Miyawaki, A. & Hofkens, J. (2005). *Proc. Natl Acad. Sci. USA*, **102**, 9511–9516.

Kelley, P. M. & Rose, L. R. F. (2002). *Prog. Mater. Sci.* **47**, 463–557.

Kneen, M., Farinas, J., Li, Y. & Verkman, A. (1998). *Biophys. J.* **74**, 1591–1599.

Langan, P. S., Close, D. W., Coates, L., Rocha, R. C., Ghosh, K., Kiss, C., Waldo, G., Freyer, J., Kovalevsky, A. & Bradbury, A. R. (2016). *J. Mol. Biol.* **428**, 1776–1789.

McCoy, A. J., Grosse-Kunstleve, R. W., Adams, P. D., Winn, M. D., Storoni, L. C. & Read, R. J. (2007). *J. Appl. Cryst.* **40**, 658–674.

Miesenböck, G., De Angelis, D. A. & Rothman, J. E. (1998). *Nature*, **394**, 192–195.

Minor, W., Cymborowski, M., Otwinowski, Z. & Chruszcz, M. (2006). *Acta Cryst.* D**62**, 859–866.

Mnyukh, Y. V., Panfilova, N. A., Petropavlov, N. N. & Uchvatova, N. S. (1975). *J. Phys. Chem. Solids*, **36**, 127–144.

Nienhaus, K., Renzi, F., Vallone, B., Wiedenmann, J. & Nienhaus, G. U. (2006). *Biophys. J.* **91**, 4210–4220.

Nihongaki, Y., Suzuki, H., Kawano, F. & Sato, M. (2014). *ACS Chem. Biol.* **9**, 617–621.

Olson, G. B. & Hartman, H. (1982). *J. Physique*, **43**, 855–865.

Otsuka, K. & Wayman, C. M. (1998). Editors. *Shape Memory Materials.* Cambridge University Press.

Regis Faro, A., Carpentier, P., Jonasson, G., Pompidor, G., Arcizet, D., Demachy, I. & Bourgeois, D. (2011). *J. Am. Chem. Soc.* **133**, 16362–16365.

Remington, S. J. (2006). *Curr. Opin. Struct. Biol.* **16**, 714–721.

Shimomura, O., Johnson, F. H. & Saiga, Y. (1962). *J. Cell. Comput. Physiol.* **59**, 223–239.

Tsien, R. Y. (1998). *Annu. Rev. Biochem.* **67**, 509–544.

Walter, A., Andresen, M., Jakobs, S., Schroeder, J. & Schwarzer, D. (2015). *J. Phys. Chem. B*, **119**, 5136–5144.
Warren, M. M., Kaucikas, M., Fitzpatrick, A., Champion, P., Timothy Sage, J. & van Thor, J. J. (2013). *Nat. Commun.* **4**, 1461.
Winn, M. D., Ballard, C. C., Cowtan, K. D., Dodson, E. J., Emsley, P., Evans, P. R., Keegan, R. M., Krissinel, E. B., Leslie, A. G. W., McCoy, A., McNicholas, S. J., Murshudov, G. N., Pannu, N. S., Potterton, E. A., Powell, H. R., Read, R. J., Vagin, A. & Wilson, K. S. (2011). *Acta Cryst.* D**67**, 235–242.
Zhou, X. X., Chung, H. K., Lam, A. J. & Lin, M. Z. (2012). *Science*, **338**, 810–814.
Zhou, X. X. & Lin, M. Z. (2013). *Curr. Opin. Chem. Biol.* **17**, 682–690.
Zimmer, M. (2002). *Chem. Rev.* **102**, 759–781.